JGR

Martian high-altitude photoelectrons independent of solar zenith angle

Shaosui Xu[1,2], Michael Liemohn[1], Stephen Bougher[1], and David Mitchell[2]

[1]Department of Climate and Space Sciences and Engineering, University of Michigan, Ann Arbor, Michigan, USA, [2]Space Sciences Laboratory, University of California, Berkeley, California, USA

Abstract Many aspects of the Martian upper atmosphere are known to vary with solar zenith angle (SZA). One would assume that dayside photoelectron fluxes are also SZA dependent, especially when transport along a semivertical magnetic field line is significant. However, our investigation presented here of the observed Martian high-altitude (~400 km) photoelectron fluxes by the magnetometer/electron reflectometer (MAG/ER) instruments on board Mars Global Surveyor (MGS) shows that the photoelectron fluxes are better correlated with just the solar irradiance, without SZA factored in, and also that the median photoelectron fluxes are independent of SZA, especially for high energies (above 100 eV). For lower energies (below 70 eV), the observed fluxes tend to vary to some degree with SZA. Such counterintuitive results are due to the existence of a photoelectron exobase, only above which the photoelectrons are able to transport and escape to high altitudes. Two methods are used here to determine the altitude range of this exobase, which varies between 145 km and 165 km depending on the atmosphere and SZA. Through our SuperThermal Electron Transport (STET) model, we found that the integral of the production rate above the photoelectron exobase, and therefore the high-altitude photoelectron fluxes, is rather independent of SZA. Such an independent relationship concerns energy redistribution in the Martian upper atmosphere, using photoelectrons to map magnetic topology and connectivity, as well as ion escape. This finding can also be carefully adapted to other solar bodies with semivertical magnetic fields at ionospheric altitudes, such as Earth, Jupiter, and Saturn.

1. Introduction

Photoelectrons, which are produced when solar photons ionize atmospheric species, are important for the dynamics and chemistry of Mars' upper atmosphere [*Schunk and Nagy*, 2009]. Most of the excess photon energy is carried away by the low-mass photoelectrons, which have kinetic energies ranging from less than 1 eV to more than 500 eV. Photoelectrons with energies above the ionization potentials of atmospheric species (13.77 eV for CO_2) can cause further ionization through electron impact. The primary and secondary electron kinetic energy is transferred to the thermal plasma through Coulomb collisions and indirectly to the neutral atmosphere through ion-neutral collisions. Eventually, these electrons lose sufficient energy to join the thermal population, which accounts for most of the ionospheric electron density. In the vicinity of the ionospheric main peak, for example, superthermal electrons account for less than 0.1% of the total electron density [e.g., *Gombosi*, 1998].

At low altitudes, where collision rates are high enough to establish photochemical equilibrium, the structure of Mars' dayside ionosphere is reasonably well described by Chapman theory [*Chapman*, 1931a, 1931b], which provides functional forms for the variation of the electron density with solar zenith angle (SZA) and altitude. The peak density is proportional to $\cos^{1/2}$(SZA), and the peak altitude, which occurs at an optical depth to ionizing radiation of unity, rises with increasing SZA from ~120 km at the subsolar point to ~180 km at the limb. A number of studies have shown at least approximate agreement between Chapman theory and measurements of ionospheric thermal electrons, including radio occultation profiles [e.g., *Hantsch and Bauer*, 1990; *Zhang et al.*, 1990; *Withers and Mendillo*, 2005; *Fox and Yeager*, 2006, 2009] and orbital radar sounding [e.g., *Nielsen et al.*, 2007; *Morgan et al.*, 2008; *Gurnett et al.*, 2008; *Němec et al.*, 2011; *Safaeinili et al.*, 2007; *Lillis et al.*, 2010]. Not all ionospheric quantities have an obvious dependence on SZA. In particular, *Withers et al.* [2014] found that the electron temperature in the main peak is independent of SZA.

At high altitudes, where collisions are infrequent, electron transport dominates, and the electron distribution is no longer described by Chapman theory. In a uniform magnetic field, electrons move along helical paths of constant radius and pitch angle, which is the angle between the particle velocity and the magnetic field. The radii of gyration for electrons with energies less than 500 eV are typically much smaller than spatial variations in the magnetic field ($\Delta B/B$), so primary photoelectrons are often magnetized, with their centers of gyration constrained to follow the magnetic field line. In addition, primary photoelectrons have an energy distribution with several discrete features, including peaks at 23 and 27 eV due to the ionization of CO_2 and O by the solar He-II line at 30.4 nm and an oxygen Auger peak at ∼500 eV. Since these features are unique to the dayside ionosphere, photoelectrons are a useful probe of topology in Mars' complex magnetic environment [e.g., *Brain et al.*, 2007; *Liemohn et al.*, 2007a].

When magnetic fields with a large vertical component are present, such as near Earth's magnetic poles and at Mars over strong crustal magnetic sources, photoelectrons are transported from where they are produced in the dayside ionosphere to altitudes of many hundreds to thousands of kilometers. Since photoelectrons travel freely only where collisions can be neglected, it is useful to consider the concept of an "electron exobase," below which collisions prevent electrons from escaping directly to high altitudes. Like the exobase of the neutral atmosphere, this is not a sharp boundary but rather a gradual transition that depends on energy and has a finite thickness [*Lillis and Fang*, 2015]. Because the photoelectron production rate decreases exponentially with increasing altitude, fluxes measured at high altitudes are dominated by production near the electron exobase (∼140–170 km), which exhibits a Chapman-like SZA dependence. Recently, photoelectron fluxes over the crustal field regions at Mars have been assumed to depend on SZA [e.g., *Liemohn et al.*, 2012; *Xu et al.*, 2014a]. In addition, *Trantham et al.* [2011] investigated the main controlling factors of photoelectrons observed by Mars Global Surveyor (MGS) and included the effects of SZA in their local EUV proxy, which they found to be the best organizer of photoelectron fluxes.

It is important to investigate if the assumed SZA effect on high-altitude photoelectrons is correct, because it concerns energy redistribution (in the form of photoelectron kinetic energy) at Mars. This is especially important for heating of the nightside atmosphere through cross-terminator transport. In addition, the escaping photoelectrons could set up ambipolar electric fields that facilitate ion escape. In this study, we examine the relationship of high-altitude photoelectrons and SZA by analyzing the measured photoelectron fluxes from the magnetometer/electron reflectometer (MAG/ER) instrument onboard Mars Global Surveyor [*Acuña et al.*, 1998; *Mitchell et al.*, 2001], accompanied by further exploration with a superthermal electron transport model.

2. Observation

In this section, we first briefly describe the data selection process. Then, we present and examine the relationship between the observed photoelectron fluxes and SZA through two different methods.

2.1. Data Selection

The MGS spacecraft was locked at 405 ± 36 km altitude and 2 A.M./P.M. local time (LT) during its mapping phase. A detailed description of the MAG/ER instrument onboard MGS is provided by *Acuña et al.* [1992]. The MAG/ER recorded electron angular distributions in sixteen 22.5° sectors with a field of view of 360° × 14°. The angular distributions can be converted into pitch angle distributions with the formula in *Mitchell et al.* [2001].

This study focuses only on photoelectrons observed within the strong crustal field regions taken during the "2 P.M. dayside" portion of the MGS orbit. To isolate dayside photoelectron samples, the same method as *Xu et al.* [2014a] is applied. The data selection is confined to SZA <90° and in a geographic box, east longitude 160°–200° and south latitude 30°–70°, as shown in Figure 1 of *Connerney et al.* [2005] and *Trantham et al.* [2011]. Within this geographic box, the strong crustal fields consist of well-defined loop arches [e.g., *Brain et al.*, 2003, 2007]. An additional magnetic field minimum strength limit of 35 nT is also applied to avoid weak fields. Furthermore, to exclude solar wind electron precipitation observations through cusps in between the magnetic loop arches, another criterion is the use of magnetic elevation angles (angle relative to the horizontal plane) within ±45° [e.g., *Xu et al.*, 2014b]. The selected electron samples range from 10 eV to 700 eV and extend over a period of more than 7 years, from early 1999 to late 2006. These criteria ensure that we are considering only dayside atmospheric photoelectrons on closed crustal field loops with direct magnetic connectivity to the photoelectron source region in the thermosphere between 100 and 200 km altitude.
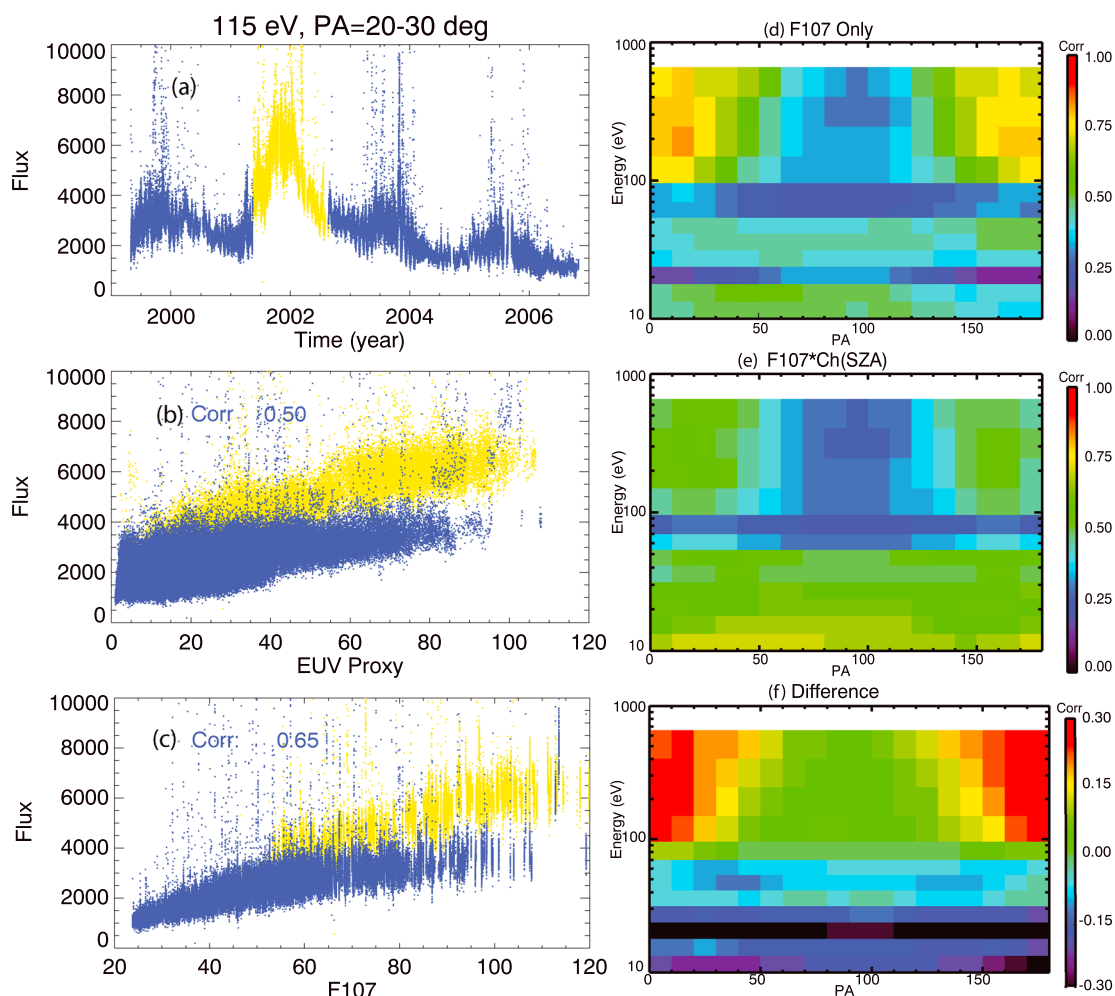
Figure 1. (a) The photoelectron fluxes (cm^{-2} eV^{-1} s^{-1} sr^{-1}) of the energy channel 115 eV at pitch angle (PA) 20°–30° observed by MGS MAG/ER against time in Earthyears. (b) The same photoelectron fluxes (cm^{-2} eV^{-1} s^{-1} sr^{-1}) in Figure 1a against EUV proxy, i.e., $F_{10.7}$ × ch(Rg, SZA). (c) The same photoelectron fluxes (cm^{-2} eV^{-1} s^{-1} sr^{-1}) in Figure 1a against $F_{10.7}$ only. In Figures 1b and 1c, the correlation of the blue fluxes and the EUV proxy and of the blue fluxes and $F_{10.7}$, respectively, is shown in the upper left corner. (d) The correlation of blue photoelectron fluxes and $F_{10.7}$ only, as a function of PA and energy. (e) The Pearson correlation coefficient of blue photoelectron fluxes and the EUV proxy. (f) The difference of the correlation coefficients of Figures 1d and 1e (Figure 1d minus Figure 1e).

2.2. SZA's Influence on Observed High-Altitude Photoelectron Fluxes

In this subsection, the relation between the observed high-altitude photoelectron fluxes and SZA is investigated through two methods. The first one compares the correlation of the photoelectron fluxes and the EUV proxy with or without SZA factored in. The other examines, for a particular solar irradiance level as indicated by Mars-adjusted $F_{10.7}$ values, how the photoelectron fluxes change with SZA. The Mars-adjusted $F_{10.7}$ values are the $F_{10.7}$ solar flux measurements at Earth compiled by NOAA being scaled to Mars according to the planet-to-Sun distances as well as the Earth-Sun-Mars angle [*Mitchell et al.*, 2001]. Also, hereinafter, only Mars-adjusted solar irradiance values are used in this study.

2.2.1. Correlation of Photoelectron Fluxes and EUV proxy

Trantham et al. [2011] investigated the main controlling factors of 27 eV photoelectron fluxes within pitch angles (PA) 80°–90° observed by MGS and concluded that the photoelectron fluxes are best correlated with their local EUV proxy. This local EUV proxy is the ratio of the solar irradiance proxy, denoted as "I_0," and a Chapman function [*Smith and Smith*, 1972] to take into account variation due to SZA, i.e., the attenuation of the solar irradiance because of a limb path. The Chapman function, ch(Rg, SZA), is a function of SZA and Rg=R/H, where R is the distance from the center of Mars and H is the scale height. This function resembles 1/cos(SZA) except for very high SZAs. The local EUV proxy is therefore $I=I_0$/ch(Rg, SZA).

The photoelectron flux is proportional to I, in contrast to the thermal electron density predicted by Chapman theory correlated to $\sqrt{I}$. The square root operator originates from the assumption that for thermal plasma, the production rate balances with the recombination rate (main loss). Such equilibrium does not apply to superthermal electrons as the recombination loss is trivial compared to other losses such as collisions with neutral particles.

Figure 1 shows an example of photoelectron fluxes of the 115 eV energy channel (a widely used energy channel [e.g., *Brain et al.*, 2007; *Lillis and Brain*, 2013]) at PA 20°–30° as a function of time in Earth year (Figure 1a), the EUV local proxy I (Figure 1b), and $F_{10.7}$ values (I_0) only (Figure 1c). Both I and I_0 are in units of sfu (solar flux unit; 1 sfu = 10^{-22} W/(m^2 Hz)) and also adjusted to Martian values. The photoelectron fluxes highlighted in yellow are for a time period that a global dust storm occurred and are much higher than the rest of the fluxes, colored in blue, even with the same EUV proxy or $F_{10.7}$ values, as shown in Figures 1b and 1c. The specialness of these yellow fluxes has been investigated by several studies [*Liemohn et al.*, 2012; *Xu et al.*, 2014a]. Hence, this study focuses only on the blue photoelectron fluxes. The correlations of these blue fluxes against the local EUV proxy and $F_{10.7}$ values only are 0.5 and 0.65, as listed in Figures 1b and 1c, respectively. Such a 0.15 enhancement of correlation is statistically significant because the correlation is calculated from hundreds of thousands of data points. Therefore, the photoelectron flux correlates better with the solar irradiance without SZA factored in.

To examine the correlations for various energies and pitch angles, Figures 1d and 1e show the correlation of the blue photoelectron fluxes against the Mars-adjusted $F_{10.7}$ values only and against the local EUV proxy, respectively, as a function of energy and PA. Figure 1f shows the difference of Figures 1d and 1e. A general improvement of correlation, for more field-aligned pitch angles in particular, is seen for energy above 70eV, up to 0.30, with SZA excluded. For energy below 70 eV, the exclusion of SZA leads to lower correlation. In other words, high-energy photoelectron fluxes observed by MGS tend to be independent of SZA, while the low-energy fluxes appear to exhibit some SZA dependence.

2.2.2. Observed Photoelectron Fluxes Against SZA

The other method is to directly examine how the photoelectron fluxes change with SZA. In Figure 2, an orbit on 16 October 2000 is chosen as an example. Figure 2 (first to eighth panels) shows north latitude, magnetic field strength, magnetic elevation angle (relative to the horizontal plane), SZA, and photoelectron fluxes at pitch angle 20°–30° for four energy channels, 313 eV, 115 eV, 47 eV, and 20 eV, against time. The longitude is about 180° for this period of time. As we can see, instead of decreasing dramatically as predicted by the Chapman function, the flux is rather constant for SZA 90°–60°. Quantitatively, the root mean square errors (RMSEs) to the mean electron flux and also to the best fitted Chapman function are calculated and shown at the upper left and lower right corners, respectively. The RMSEs of the mean value are 2–3 times smaller than that of the Chapman function for all the energy channels. This implies that a straight-line fit is substantially better than the SZA-dependent Chapman function fit to these data.

In addition to this case study, we present another statistical examination of the relation between the photoelectron flux and SZA. The blue fluxes in Figure 1a are divided into eight Mars-adjusted $F_{10.7}$ levels and eight SZA bins. Then for the same $F_{10.7}$ level, the median flux of each SZA bin is normalized by the maximum of these median fluxes. Normalized median photoelectron fluxes at pitch angles 20°–30° against SZA are shown in Figure 3 with different colors highlighting different $F_{10.7}$ levels. The four rows, from top to bottom, are for energy channels 313 eV, 115 eV, 47 eV, and 20 eV, respectively. Figures 3a–3d show the normalized median flux for each $F_{10.7}$ level. For Figures 3e–3h, three $F_{10.7}$ levels are selected, highlighted in three different colors and line styles. For each color and line style, there are three lines marking the quartile values for the normalized flux. The median photoelectron fluxes across all the solar zenith angle bins mostly vary within 80% from the maximum of these median fluxes for energies above 30 eV for all the pitch angles, as shown in Figures 3a–3c. Only the energy channel below 30 eV exhibits a more systematic flux decrease at high SZAs, e.g., in Figure 3d. Similarly, the calculated RMSEs to the mean flux are much smaller, by a factor of 2 to more than 10, than that to the fitted Chapman function, except for the 20 eV energy channel with $F_{10.7} = 43$ sfu.

Again, an independence of the photoelectron fluxes on SZA is seen for energy above 30 eV. In contrast, the photoelectron flux does decrease significantly with increasing SZA below 30 eV. This finding is consistent with the other method, even though the energy cutoff differs.
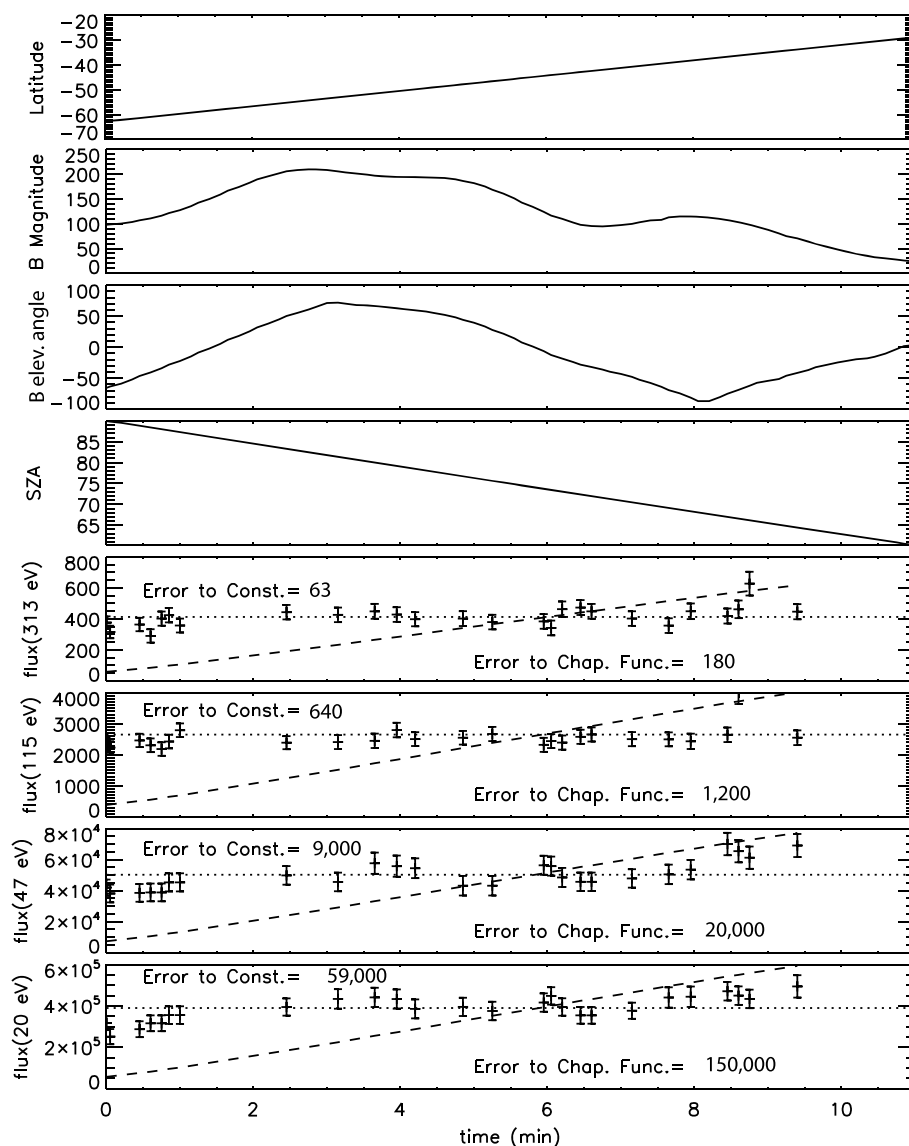
Figure 2. One orbit example: MGS data for 16 October 2000, the *x* axis is the time in minutes, starting from UT 17:27:50. (first panel) MGS location over Mars in latitude (deg); (second panel) the magnitude of the magnetic fields (nT); (third panel) the elevation angle of the magnetic fields (deg); (fourth panel) MGS solar zenith angle (deg); and (fifth to eighth panels) differential number fluxes (eV^{-1} cm^{-2} s^{-1} sr^{-1}) for four energy channels centered at 313 eV, 115 eV, 47 eV, and 20 eV, respectively, at PA 20°–30°. The longitude is around 180°. The dotted lines in Figure 2 (fifth to eighth panels) mark the mean flux, and the dashed lines are for the best fitted Chapman function. The standard errors to the mean photoelectron flux and the best fitted Chapman function are shown at the upper left and lower right corners, respectively.

3. Simulations

Such a relationship between the high-altitude photoelectron fluxes and SZA, even somewhat energy dependent, is rather counterintuitive and demands a closer examination. Therefore, we employ a superthermal electron transport model to explore this puzzle. In this section, first a brief description of the SuperThermal Electron Transport (STET) model is given. Then, we show that the model is able to replicate photoelectron fluxes being independent of SZA at 400 km and the explanation of such independence is also discussed.

3.1. STET Model Results

The STET model solves the gyration-averaged Boltzmann kinetic equation to calculate the superthermal electron flux distribution along a magnetic flux tube. This multistream model was originally developed for
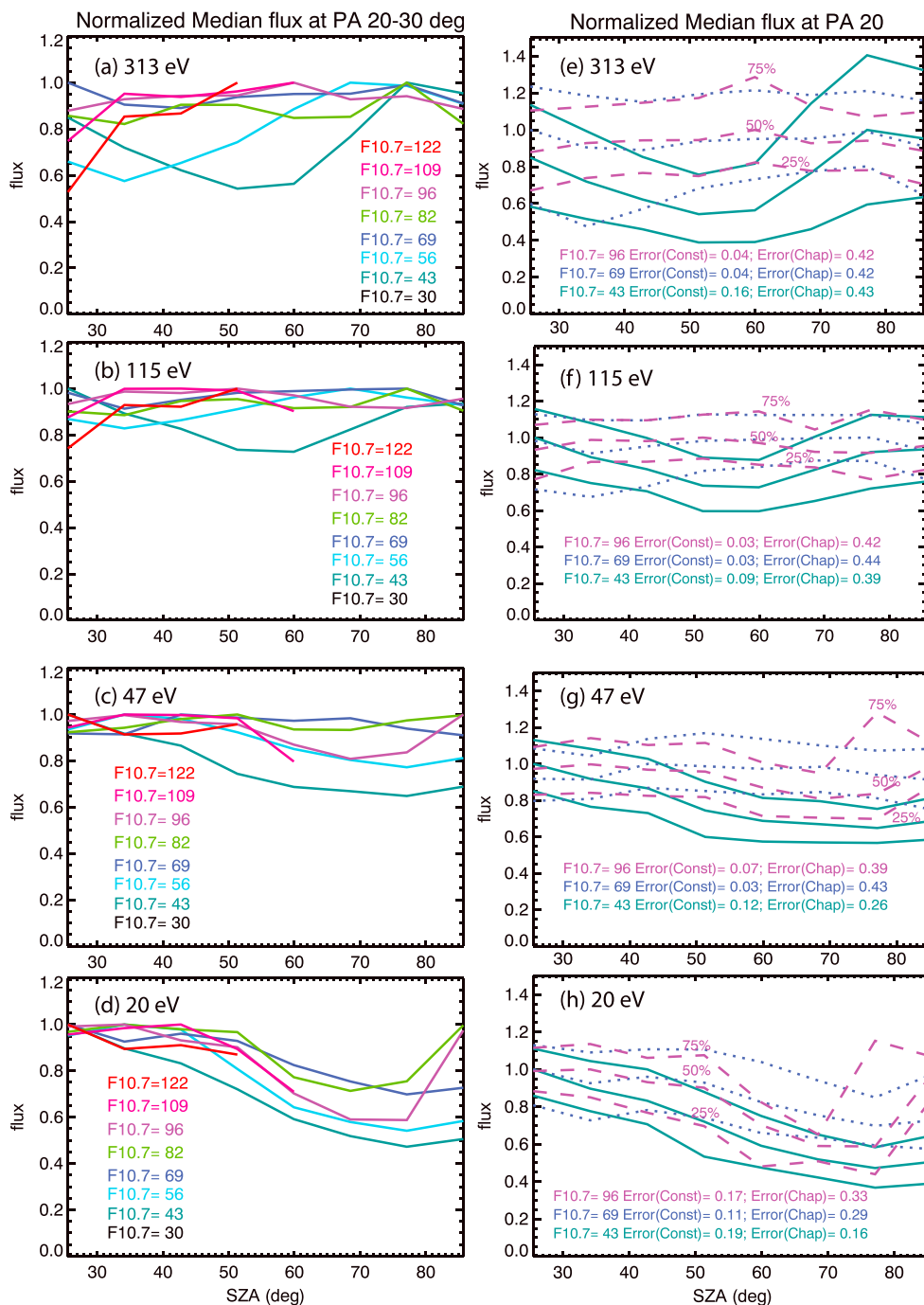
Figure 3. Normalized median photoelectron flux at pitch angles 20°–30° against SZA with colors showing different $F_{10.7}$ levels. For each $F_{10.7}$ level, the median fluxes are normalized by the maximum of all the SZA bins. The energy channels: (a, e) 313 eV, (b, f) 115 eV, (c, g) 47 eV, and (d, h) 20 eV. Figures 3a–3d show the normalized median flux for each $F_{10.7}$ level. For Figures 3e–3h, three $F_{10.7}$ levels are selected, highlighted in three different colors and line styles: dark green solid lines for $F_{10.7} = 43$ sfu, blue dot lines for $F_{10.7} = 69$ sfu, and purple dashed lines for $F_{10.7} = 96$ sfu. For each color and line style, there are three lines marking the quartile values, 25%, 50%, and 75%, of the normalized flux.
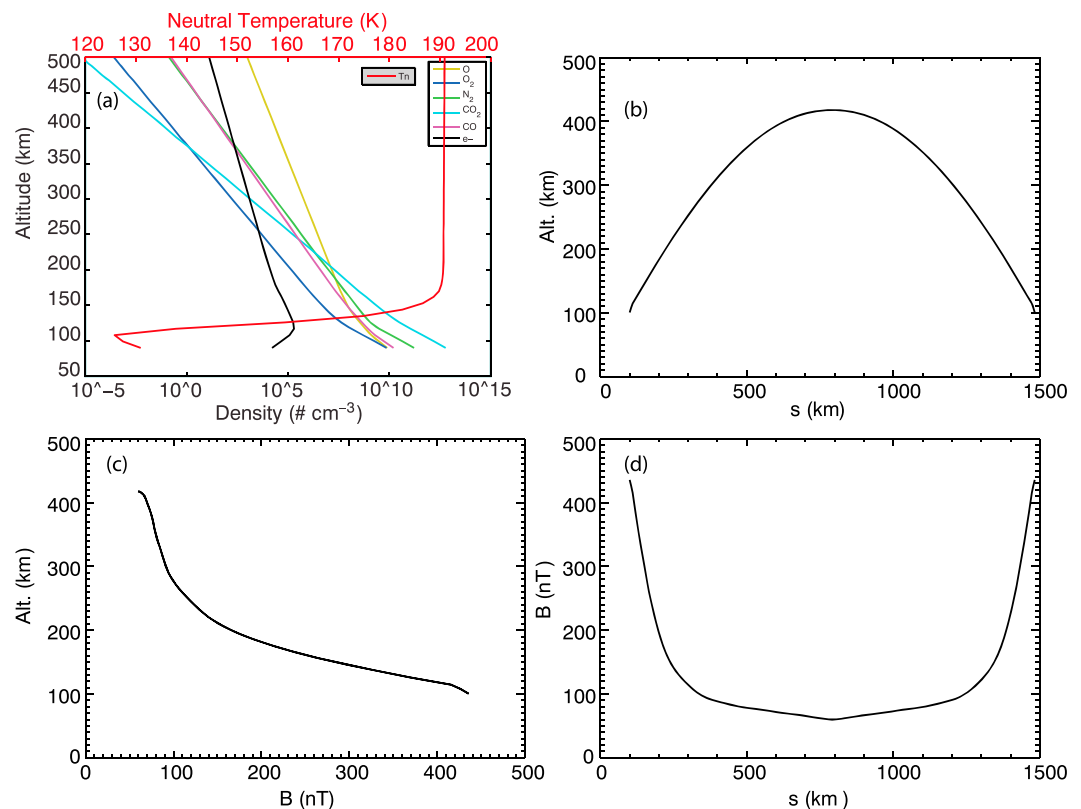
Figure 4. (a) Neutral densities, thermal electron density, and neutral temperature at solar zenith angle (SZA) of 0° of Mars from MTGCM against altitude; (b) B field line altitudes against distance s; (c) B field strength against altitude; and (d) B field strength against distance s.

the Earth environment [*Khazanov et al.*, 1993; *Khazanov and Liemohn*, 1995; *Liemohn et al.*, 1997] and later modified for Mars [*Liemohn et al.*, 2003, 2006]. *Xu and Liemohn* [2015] provides the detailed description of the STET model. The flux is in the coordinate system [t, E, μ, s], where t is time; E is the electron energy in eV; μ is the cosine of the local pitch angle; and s is the distance along the local magnetic field line. The STET model is equipped with several solar irradiance models [*Xu et al.*, 2015a], including the Hinteregger-81 model [*Hinteregger et al.*, 1981], the Flare Irradiance Spectral Model (FISM) [*Chamberlin et al.*, 2007, 2008], and the Heliospheric Environment Solar Spectral Radiation (HESSR) model [*Fontenla et al.*, 2009]. In addition, the photoionization and excitation cross sections are from *Fox* [1991], and the electron impact cross sections from *Sung and Fox* [2000]. The neutral and ionospheric plasma density profiles are from the Mars Thermospheric General Circulation Model (MTGCM) [*Bougher et al.*, 1999, 2000, 2001, 2004, 2006] for the altitude range of 100–240 km and linearly extrapolated from the logarithm of the two topmost values from MTGCM above 240 km.

The solar irradiance model used for this study is the Hinteregger-81 model. All three models will have the same dependence on SZA with respect to the local photoelectron production rate, and therefore this choice is purely for convenience. The background neutral and plasma environment based on MTGCM, run at a solar longitude Ls of 90° with an Earth $F_{10.7}$ of 100 sfu (roughly 43 sfu at Mars), for this study is shown in Figures 4 and 5, along with the magnetic configuration. A Mars $F_{10.7}$ of 43 sfu is also used for the Hinteregger-81 model, and the Mars-Sun distance is 1.524 AU. Below, we will only present $F_{10.7}$ values that have been converted into Mars. The s step size is 5 km below 200 km and 10 km above 200 km, to ensure that it is no larger than the neutral scale height. The pitch angle grid number at the minimum B value along the field line is 20 for 0°–90° for the superthermal electron flux along the magnetic direction and 20 for 90°–180° for the flux flowing in the opposite direction. A uniform energy grid size of 1eV is used for 1–200 eV. All the runs for this study are in steady state, considered converged as $|\psi - \psi_{last}|/\psi < 0.02$, where ψ and ψ_{last} are the electron flux at the current time step and the last time step at every location in the s-μ-E grid, respectively.
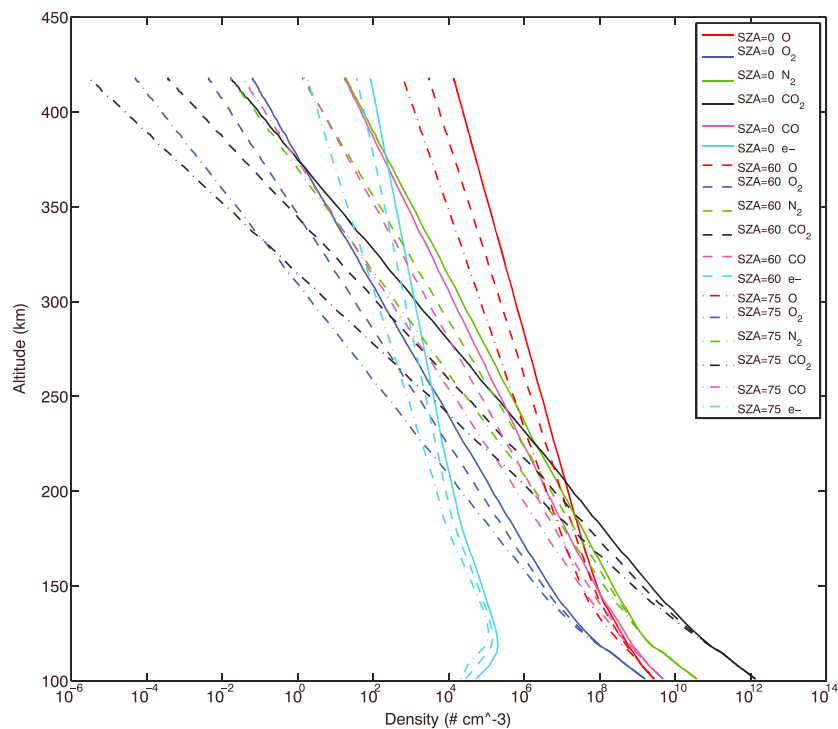
Figure 5. Neutral densities and thermal electron density of Mars from MTGCM against altitude at three SZAs: 0°, 60°, and 75°. Different colors are for different species' density profiles, red for O, blue for O_2, green for N_2, black for CO_2, purple for CO, and light blue for electron, while different line styles are for different SZAs, solid for 0°, dashed for 60°, and dash-dot-dotted for 75°.

The photoelectron fluxes vary with solar zenith angle because of two reasons. One is that the attenuation of the solar irradiance is larger with increasing SZA due to the slant path. The other is that the atmospheric densities and temperatures change with SZA. Hence, in this section, we will first use the same atmosphere (the atmosphere at SZA = 0°, as shown in Figure 4a) to simulate at 10 SZAs, from 0° to 90°. Then, we will run STET with two extra atmospheres, at SZA = 60° and at SZA = 75°, as shown in Figure 5, to discuss how different atmospheres influence the results.

Figures 6a–6d show the photoelectron fluxes at PA = 0° at different altitudes against SZA for 20 eV, 50 eV, 100 eV, and 190 eV, respectively. The solid lines are for 10 runs with the same atmosphere and the triangle symbols for STET runs at different SZAs with the corresponding atmospheres. For the runs with the same atmosphere, the photoelectron fluxes decrease as SZA increases at 130 km. For comparison, the dotted lines show the fluxes at SZA = 0 and 130 km altitude divided by the Chapman function, ch(Rg, SZA). The disagreement between the modeled fluxes at SZA = 90° at 130 km (black solid line) and the Chapman function scaling is because this scaling is for peak densities but not at a particular altitude. For altitudes above 150 km, the photoelectron fluxes are almost constant across all SZAs, with a slight decrease at SZA = 90°. For the runs with different atmospheres, the fluxes are mostly constant with respect to SZA for all the altitudes as well. Therefore, the modeled photoelectron fluxes also show independence on the solar zenith angle, which is consistent with the observations from section 2.

3.2. Why: The Superthermal Electron Exobase

The reason of this independence is the existence of a critical altitude range for photoelectrons, only above which photoelectrons can transport/escape instead of losing energy locally [e.g., *Banks and Nagy*, 1970; *Butler and Stolarski*, 1978; *Mantas and Hanson*, 1979]. The measurements over the strong crustal fields made by MGS (∼400 km), well above the main region of the ionosphere, should be mainly the transport-dominated population. So it is necessary to determine this altitude range. In this study, we provide two approaches.
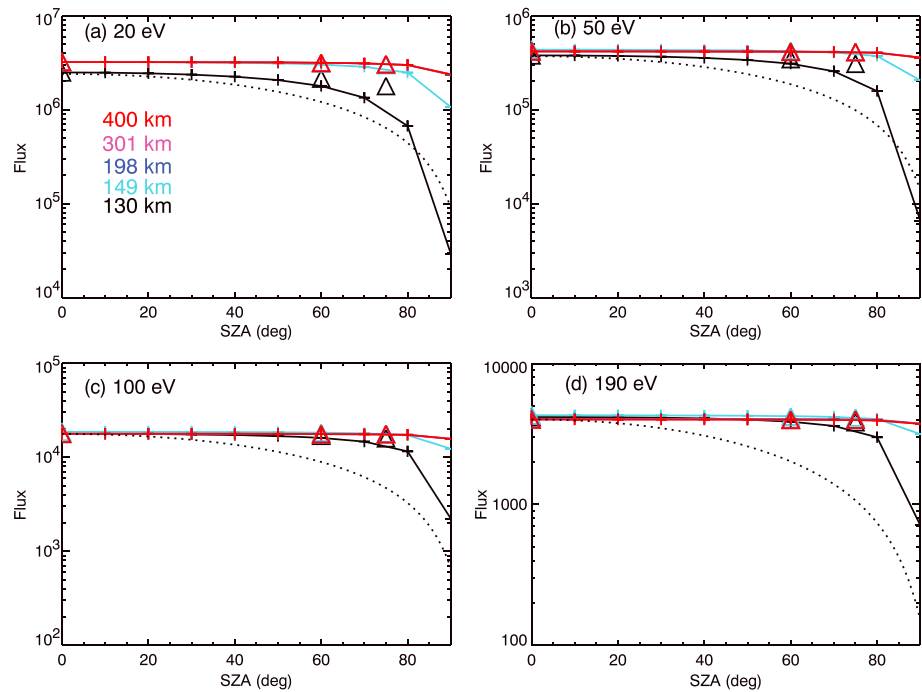
Figure 6. The flux (cm^{-2} eV^{-1} s^{-1} sr^{-1}) at PA 0 against SZA at different altitudes, highlighted in different colors, for (a) 20 eV, (b) 50 eV, (c) 100 eV, and (d) 190 eV, with the dotted line showing fluxes scaled by the Chapman function. The solid lines with crosses are for the 10 runs with the same atmosphere, and the triangle symbols are for the three atmospheres.

The first approach is to use the formula provided by *Banks and Nagy* [1970], which defines the photoelectron mean free path λ as

$$\lambda = \frac{\langle \cos \theta \rangle \sin \alpha}{n \sqrt{\sigma_a (\sigma_a + 2p_e \sigma_e)}}, \tag{1}$$

where $\langle \cos \theta \rangle$ is the averaged pitch angle distribution; α is the dip angle of the magnetic field line, relative to the horizontal plane; n is the neutral density; σ_a and σ_e are the inelastic and elastic collision cross sections with neutrals, respectively; and p_e is the backscatter probability for the elastic collisions. When $\lambda \ll H$, where H is the scale height, there is little to no net transport and photoelectrons lose energy locally, while above the altitude where $\lambda \simeq H$, photoelectron transport becomes significant. Here we generalize this formula to the multispecies case by changing the denominator in equation (1) to $\sum_i n_i \sqrt{\sigma_{ai}(\sigma_{ai} + 2p_{ei}\sigma_{ei})}$, where i indicates the ith neutral species. For our calculation, α is near 90° below 200 km, and $\langle \cos \theta \rangle = 0.5$, as it ranges from 3/8 to 9/16 [*Banks and Nagy*, 1970]. The photoelectron mean free path λ against altitude, along with the neutral scale height H, calculated as a weighted average of all atmospheric species (black dashed line), is shown in Figure 7a. The altitudes at which $\lambda = H$ for different energies range from 160 to 165 km for the MTGCM atmosphere at SZA = 0° and from 150 to 155 km for the MTGCM atmosphere at SZA = 75°. For convenience, we define the "photoelectron exobase" as the altitude of $\lambda = H$. However, it is important to note that it is not immediately collisionless above this exobase. Instead, there is a transition region in which transport dominates but collisions still happen. The photoelectron exobase is at lower altitudes than the exobase of the neutral atmosphere, which is located above 200 km, because these high-energy electrons' collision cross sections are much smaller than the neutral particles.

Another approach to determine this photoelectron exobase is to calculate a "collisional depth" τ, similar to the optical depth, for a superthermal electron moving downward from the top of the upper atmosphere:

$$\tau = \int_{z(s)}^{z_{max}} \sum_j n_j p_j \sigma_j \, ds \tag{2}$$

where σ_j can be the cross section of inelastic and elastic collisions with the jth neutral species, as well as the Coulomb collision cross sections with electrons; n_j is the corresponding density; p_j is the backscatter
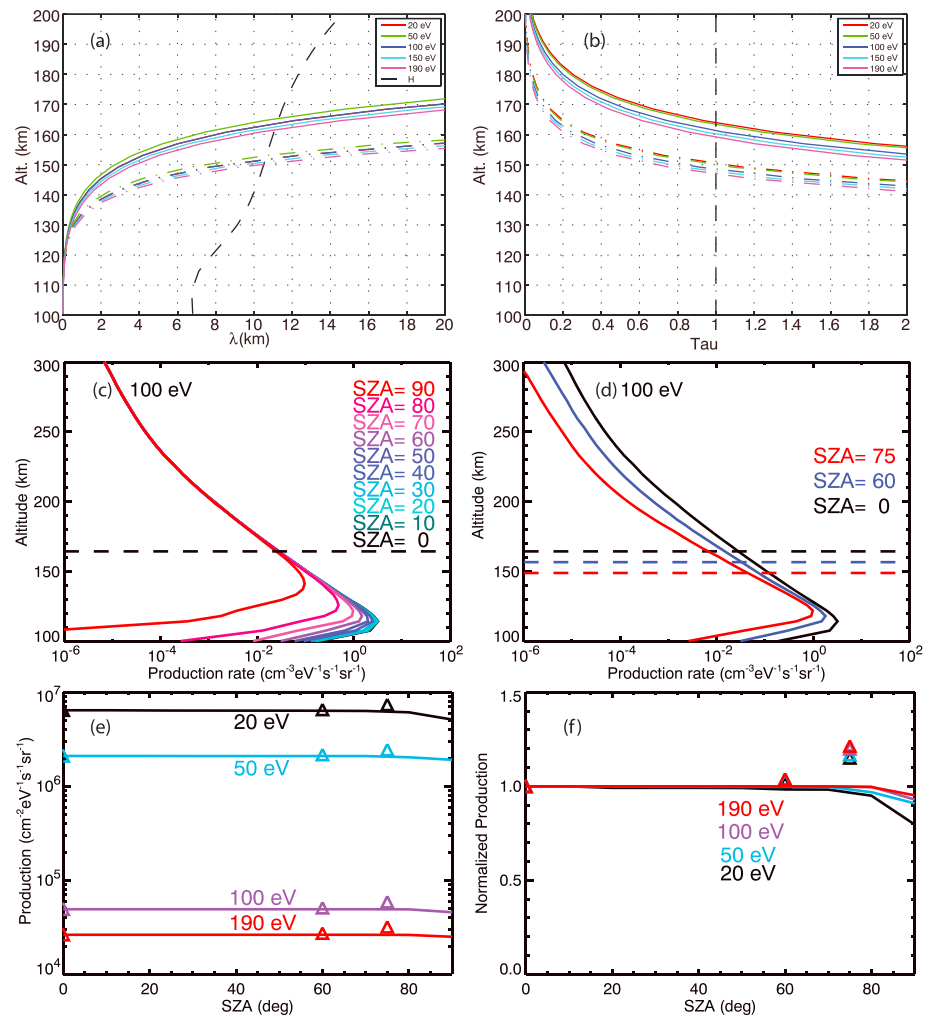
Figure 7. (a) λ and (b) τ against altitude. Different colors are for different energies. The solid lines are for the MTGCM atmosphere at SZA=0° and the dash-dotted lines for SZA=75°. The dashed black line in Figure 7a is the scale height (*H*) against altitude. The dashed black line in Figure 7b marks $\tau=1$. (c) The photoelectron production rate (cm^{-2} eV^{-1} s^{-1} sr^{-1}) from the same atmosphere, against altitude for 100 eV. Different colors highlight different SZAs. The horizontal dashed line marks the photoelectron exobase. (d) The photoelectron production rate (cm^{-2} eV^{-1} s^{-1} sr^{-1}) from the three MTGCM atmospheres (SZA=0°, 60°, 75°) against altitude for 100 eV. The dashed lines show the exobases for three atmospheres. (e) Integrated production rate (cm^{-2} eV^{-1} s^{-1} sr^{-1}) above the exobase against SZA for different energies. The solid lines are for the 10 runs with the same atmosphere, and the symbols are for the three atmospheres. (f) Integrated production rate normalized by the production rate at SZA=0° against SZA for different energies, the same format as in Figure 7e.

probability for the elastic collision with neutrals and 1 for other collisions. Also, in equation (2), *s* is the distance along the field line. The electron-ion collision term is neglected as the effect is small compared to electron-neutral and electron-electron collisions. Note that τ is a unitless integral from the highest altitude z_{max} of the field line to a certain altitude $z(s)$ and stands for the probability of one photoelectron not being able to transport from the top of field line to $z(s)$, or vice verse, from $z(s)$ to the top of the field line. In other words, only when $\tau \leq 1$ can photoelectrons be transported to high altitudes; otherwise, they are lost locally or to nearby altitudes. Figure 7b shows τ of different energies against altitude. $\tau=1$ happens at the 160–165 km altitude range for the MTGCM atmosphere at SZA=0° and at the 147–152 km range for the MTGCM atmosphere at SZA=75°, which is consistent with the previous method.

For the 10 runs with the same atmosphere, the calculated photoionization production rate against altitude at different SZAs for 100 eV is shown in Figure 7c. The peak production rate decreases and the peak altitude increases as SZA increases, as Chapman theory predicted. However, above the photoelectron exobase,

marked by the dashed black line, the production rates are about the same for all the SZAs. Then, for the three runs with a consistent atmosphere and SZA, the photoionization rates against altitude for the three SZAs are shown in Figure 7d, and the dashed lines are the calculated exobases. While the production rate decreases with increasing SZA, as expected, the exobase moves to lower altitudes, because the atmosphere is less dense.

To further demonstrate the effect of this photoelectron exobase, we integrated the photoionization production rate from the exobase to the highest altitude z_{max} of the field line for each SZA, as shown in Figure 7e. The solid lines are for 10 runs with the same atmosphere, while the triangle symbols are for STET runs at different SZAs with the corresponding atmospheres. In addition, Figure 7f shows the normalization of this photoionization production rate integral against SZA, calculated by dividing by the values at SZA = 0°. For the 10 runs with the same atmosphere, an almost constant photoionization production rate integral, with a slight decrease at high SZAs, is seen, while for the runs with different atmospheres, the production rate integral increases slightly at higher SZAs, as the exobase altitude decreases. In other words, in both sets of the simulations, with or without changing atmospheres, the photoionization production rate integral is fairly constant across all the SZAs.

4. Discussion and Conclusions

Photoelectron fluxes over the strong crustal field regions at Mars were assumed to change with solar zenith angle because they are directly connected to the source region below 200 km altitude. If part of the photoelectrons produced at the peak altitude transport to high altitudes along closed magnetic fields, then the photoelectron fluxes should scale, though maybe not linearly, with the peak values. However, through our examination of the MGS MAG/ER data over the strong crustal fields, the high-altitude photoelectron fluxes are better correlated with solely the solar irradiance, without SZA factored in, especially for the high energies. Furthermore, in addition to a case study as an example, the median photoelectron fluxes across all the solar zenith angle bins mostly vary within 80% from the maximum of these median fluxes for the same Mars-adjusted $F_{10.7}$ level. Plus, through the calculation of root mean square errors, the observed photoelectron flux is better described by a constant value against SZA rather than a Chapman function best fitted curve, indicating an independence.

The STET model is able to replicate the independence of high-altitude photoelectron fluxes against SZA. Below the photoelectron exobase, while the peak fluxes vary roughly as the inverse of ch(Rg, SZA), these photoelectrons are lost locally due to collisions. Only above this exobase, locally and freshly produced photoelectrons are able to transport to high altitudes. It was found that the photoelectron exobase is located between 145 and 165 km altitude, which is below the neutral atmosphere exobase because of the smaller collision cross section of these fast-moving particles. In addition, this value is in reasonable agreement with *Mantas and Hanson* [1979], who found that photoelectron transport starts to be significant in the 130–150 km altitude range. Similarly, *Lillis et al.* [2008] determined that the scattering probability for 191 eV precipitating electrons at PA <24° reaches 1 at ∼160 km, which also supports our results. The analysis of the photoionization production rate from the simulation indicates that, above the photoelectron exobase, the integral of the production rate barely changes with SZA. As a result, high-altitude photoelectron fluxes are rather independent of the changing of the peak values when the peak altitude is several scale heights below the photoelectron exobase.

This result does not change when different atmospheres are used. In this study, we have tested three different atmospheres, taking into account the location difference, for the same $F_{10.7}$ level. While the production rate changes with different atmospheres (Figure 7d), the production rate integral above the exobases, however, remains the same as the exobase varies in altitude for different atmospheres (Figures 7e and 7f). On the other hand, the observations are a collection of 7 years of data, spanning all the seasons and different solar irradiance strengths. The statistical approach of section 2.2.1 should average over the variations of the seasons and solar cycle changes. Also, the median fluxes are independent of SZA for all the observed $F_{10.7}$ levels, which implies that this finding is applicable to different solar irradiance fluxes and that the atmospheres we used are appropriate and adequate.

There are a couple of caveats in this study. For example, there are uncertainties with adjusting $F_{10.7}$ from Earth to Mars to use as a proxy [e.g., *Peterson et al.*, 2013]. However, the statistical approaches used in this study should largely reduce the errors due to this approximation. Furthermore, the model demonstrates that with

the same solar irradiance level, the photoelectron fluxes vary little with SZA, which validates the observational results. Another caveat is that the data sample is confined to the closed crustal field loops. A closed field line has two foot points with two production regions near the main peak being separated by 10° or more of solar zenith angle. Thus, a lack of SZA dependence by the observation could be partially caused by this smearing effect. However, our model simulations give the same SZA for both legs so that there is no smearing effect. Yet the model results illustrate that the photoelectron fluxes are independent of SZA. From the modeling results, the production integral above the superthermal electron exobase is independent of SZA; therefore, such a smearing effect should make little difference. With modeling, we are able to simulate more controlled environments to determine the underlying physics.

It is also interesting to take a closer examination of the observational results of high-energy photoelectrons in Figure 1f. The enhanced correlation is more prominent for more field-aligned pitch angles than perpendicular pitch angles. For pitch angles near 90°, the photoelectron fluxes observed at 400 km are mostly scattered into these pitch angles, as electrons' perpendicular velocities decrease with weakening magnetic strength, to conserve the first adiabatic invariant. In other words, these fluxes rely on not only the source but also the scattering processes at high altitudes, such as collisions with neutral particles or thermal electrons. This comparison of field-aligned and perpendicular pitch angles indicates a source change, consistent with our explanation. Also, the higher the energy, the more pitch angle bins show an increase in the correlation coefficient. The collision cross sections are lower with increasing energy, and therefore photoelectron fluxes are less affected by collision processes but more controlled by the source changes.

The modeled low-energy photoelectron fluxes remain quite constant through all the SZAs, with a slight drop of fluxes at SZA~90°, at high altitudes. In contrast, the photoelectron fluxes observed by the MGS spacecraft show some dependence on SZA for low energies, even though the energy cutoff is different for the two approaches in section 2. From our model results, the peak altitudes are generally closer to the exobase for low energies than high energies (not shown). It is also suggested in Figure 7f, where the normalized production rate decreases more at high SZA for lower energies. It is possible that in reality, the photoelectron exobase is systematically closer to the peak altitudes than what our model predicts. In such a case, the low-energy photoelectrons will be partially controlled by SZA. Another possibility of the discrepancy between the observation and the model results is that the sources and losses for low-energy photoelectrons are more complicated than the high energies. Cascading and secondary electrons are also important sources, while the loss due to Coulomb collisions is more prominent at the low-energy range. Therefore, the low-energy photoelectron fluxes depend on more parameters, such as the thermal electron density profile, so that it is harder to replicate by the simple model setup used here. Finally, the quality of the electron data for low-energy channels from the MGS spacecraft might be not very good so that the findings of the low-energy channels are questionable. The low-energy channels are easily contaminated in some ER anode sectors by spacecraft photoelectrons.

In summary, we have shown that high-altitude photoelectron fluxes over Martian strong crustal field regions are rather independent of solar zenith angle, especially for high energies. This finding has a few implications. First, it implies that the energy carried by photoelectrons transported to nightside probably varies little regardless of where the photoelectrons come from. Superthermal electrons are considered as the main energy source to the Martian nightside, causing heating, ionization, and excitation (probably aurora [e.g., *Bertaux et al.*, 2005; *Brain et al.*, 2006; *Leblanc et al.*, 2008]). Our study suggests that it should not be assumed that less energy is carried by photoelectrons transported along close magnetic field lines that straddle the terminator [e.g., *Liemohn et al.*, 2007a] or along purely dayside closed field lines with foot points at very different SZAs. Also, high-altitude photoelectrons are observed and modeled within the Martian tail [*Liemohn et al.*, 2006, 2007b; *Frahm et al.*, 2006a, 2006b]. *Frahm et al.* [2010] estimated a Martian photoelectron escape rate of ~3 × 10²³ s⁻¹, which was compared with ion escape estimations. *Frahm et al.* [2010] and *Coates et al.* [2011] suggest that these escaping photoelectrons may at least partially contribute to Martian atmospheric loss. In particular, these photoelectrons can set up ambipolar electric fields that facilitate ion escape along open magnetic fields. Our study implies that such an effect is probably the same for open field lines at all SZAs. On the other hand, this study also discourages the possibility of using the escaping photoelectron fluxes on an open magnetic field to infer the location of the footprint of this field line, as there is no SZA dependence, and therefore the source region cannot be specifically identified. Furthermore, as shown in this study, the properties of photoelectrons above the photoelectron exobase can be quite counterintuitive and should be treated with extra care. For example, *Xu et al.* [2015b] show that the above this exobase, the high-altitude photoelectron

fluxes are independent of the total neutral density at field-aligned pitch angles but very sensitive to composition changes. With the new data from Mars Atmosphere and Volatile EvolutioN (MAVEN) [*Jakosky et al.*, 2015], it is critical to take into account the observation altitudes relative to this exobase to employ the correct analysis. Finally, such an independence should be expected at planets for which vertical transport can be significant, such as Earth, Jupiter, and Saturn, but detailed analysis is required to verify this generalization.

References

Acuña, M., et al. (1992), Mars observer magnetic fields investigation, *J. Geophys. Res.*, *97*(E5), 7799–7814.

Acuña, M., et al. (1998), Magnetic field and plasma observations at Mars: Initial results of the Mars Global Surveyor mission, *Science*, *279*(5357), 1676–1680.

Banks, P., and A. Nagy (1970), Concerning the influence of elastic scattering upon photoelectron transport and escape, *J. Geophys. Res.*, *75*(10), 1902–1910.

Bertaux, J.-L., F. Leblanc, O. Witasse, E. Quemerais, J. Lilensten, S. Stern, B. Sandel, and O. Korablev (2005), Discovery of an aurora on Mars, *Nature*, *435*(7043), 790–794.

Bougher, S. W., S. Engel, R. Roble, and B. Foster (1999), Comparative terrestrial planet thermospheres: 2. Solar cycle variation of global structure and winds at equinox, *J. Geophys. Res.*, *104*(E7), 16,591–16,611.

Bougher, S. W., S. Engel, R. Roble, and B. Foster (2000), Comparative terrestrial planet thermospheres: 3. Solar cycle variation of global structure and winds at solstices, *J. Geophys. Res.*, *105*(E7), 17,669–17,692.

Bougher, S. W., S. Engel, D. P. Hinson, and J. M. Forbes (2001), Mars Global Surveyor radio science electron density profiles: Neutral atmosphere implications, *Geophys. Res. Lett.*, *28*, 3091–3094, doi:10.1029/2001GL012884.

Bougher, S. W., S. Engel, D. Hinson, and J. Murphy (2004), MGS Radio Science electron density profiles: Interannual variability and implications for the Martian neutral atmosphere, *J. Geophys. Res.*, *109*, E03010, doi:10.1029/2003JE002154.

Bougher, S. W., J. Bell, J. Murphy, M. Lopez-Valverde, and P. Withers (2006), Polar warming in the Mars thermosphere: Seasonal variations owing to changing insolation and dust distributions, *Geophys. Res. Lett.*, *33*, L02203, doi:10.1029/2005GL024059.

Brain, D., F. Bagenal, M. Acuña, and J. Connerney (2003), Martian magnetic morphology: Contributions from the solar wind and crust, *J. Geophys. Res.*, *108*(A12), 1424, doi:10.1029/2002JA009482.

Brain, D., J. Halekas, L. Peticolas, R. Lin, J. Luhmann, D. Mitchell, G. Delory, S. Bougher, M. Acuña, and H. Rème (2006), On the origin of aurora on Mars, *Geophys. Res. Lett.*, *33*, L01201, doi:10.1029/2005GL024782.

Brain, D., R. Lillis, D. Mitchell, J. Halekas, and R. Lin (2007), Electron pitch angle distributions as indicators of magnetic field topology near Mars, *J. Geophys. Res.*, *112*, A09201, doi:10.1029/2007JA012435.

Butler, D. M., and R. S. Stolarski (1978), Photoelectrons and electron temperatures in the Venus ionosphere, *J. Geophys. Res.*, *83*(A5), 2057–2065.

Chamberlin, P. C., T. N. Woods, and F. G. Eparvier (2007), Flare Irradiance Spectral Model (FISM): Daily component algorithms and results, *Space Weather*, *5*, S07005, doi:10.1029/2007SW000316.

Chamberlin, P. C., T. N. Woods, and F. G. Eparvier (2008), Flare Irradiance Spectral Model (FISM): Flare component algorithms and results, *Space Weather*, *6*, S05001, doi:10.1029/2007SW000372.

Chapman, S. (1931a), The absorption and dissociative or ionizing effect of monochromatic radiation in an atmosphere on a rotating Earth, *Proc. Phys. Soc.*, *43*, 26–45, doi:10.1088/0959-5309/43/1/305.

Chapman, S. (1931b), The absorption and dissociative or ionizing effect of monochromatic radiation in an atmosphere on a rotating Earth part II. Grazing incidence, *Proc. Phys. Soc.*, *43*, 483–501, doi:10.1088/0959-5309/43/5/302.

Coates, A. J., S. Tsang, A. Wellbrock, R. Frahm, J. Winningham, S. Barabash, R. Lundin, D. Young, and F. Crary (2011), Ionospheric photoelectrons: Comparing Venus, Earth, Mars and Titan, *Planet. Space Sci.*, *59*(10), 1019–1027.

Connerney, J., M. Acuña, N. Ness, G. Kletetschka, D. Mitchell, R. Lin, and H. Reme (2005), Tectonic implications of Mars crustal magnetism, *Proc. Natl. Acad. Sci. U.S.A.*, *102*(42), 14,970–14,975.

Fontenla, J. M., E. Quémerais, I. González Hernández, C. Lindsey, and M. Haberreiter (2009), Solar irradiance forecast and far-side imaging, *Adv. Space Res.*, *44*, 457–464, doi:10.1016/j.asr.2009.04.010.

Fox, J. L. (1991), Cross sections and reaction rates of relevance to aeronomy, *Rev. Geophys.*, *29*, 1110–1131.

Fox, J. L., and K. E. Yeager (2006), Morphology of the near-terminator Martian ionosphere: A comparison of models and data, *J. Geophys. Res.*, *111*, A10309, doi:10.1029/2006JA011697.

Fox, J. L., and K. E. Yeager (2009), MGS electron density profiles: Analysis of the peak magnitudes, *Icarus*, *200*, 468–479, doi:10.1016/j.icarus.2008.12.002.

Frahm, R., et al. (2006a), Locations of atmospheric photoelectron energy peaks within the Mars environment, *Space Sci. Rev.*, *126*(1–4), 389–402.

Frahm, R., et al. (2006b), Carbon dioxide photoelectron energy peaks at Mars, *Icarus*, *182*(2), 371–382.

Frahm, R., et al. (2010), Estimation of the escape of photoelectrons from Mars in 2004 liberated by the ionization of carbon dioxide and atomic oxygen, *Icarus*, *206*(1), 50–63.

Gombosi, T. I. (1998), *Physics of the Space Environment*, Cambridge Univ. Press, Cambridge, U. K.

Gurnett, D. A., et al. (2008), An overview of radar soundings of the Martian ionosphere from the Mars Express spacecraft, *Adv. Space Res.*, *41*, 1335–1346, doi:10.1016/j.asr.2007.01.062.

Hantsch, M., and S. Bauer (1990), Solar control of the Mars ionosphere, *Planet. Space Sci.*, *38*(4), 539–542.

Hinteregger, H. E., K. Fukui, and B. R. Gilson (1981), Observational, reference and model data on solar EUV, from measurements on *AE-E*, *Geophys. Res. Lett.*, *8*, 1147–1150, doi:10.1029/GL008i011p01147.

Jakosky, B. M., et al. (2015), The Mars Atmosphere and Volatile Evolution (MAVEN) Mission, *Space Sci. Rev.*, *195*, 3–48.

Khazanov, G., and M. Liemohn (1995), Nonsteady state ionosphere-plasmasphere coupling of superthermal electrons, *J. Geophys. Res.*, *100*(A6), 9669–9681.

Khazanov, G. V., M. W. Liemohn, T. I. Gombosi, and A. F. Nagy (1993), Non-steady-state transport of superthermal electrons in the plasmasphere, *Geophys. Res. Lett.*, *20*, 2821–2824, doi:10.1029/93GL03121.

Leblanc, F., et al. (2008), Observations of aurorae by SPICAM ultraviolet spectrograph on board Mars Express: Simultaneous ASPERA-3 and MARSIS measurements, *J. Geophys. Res.*, *113*, A08311, doi:10.1029/2008JA013033.

Liemohn, M., G. Khazanov, T. Moore, and S. Guiter (1997), Self-consistent superthermal electron effects on plasmaspheric refilling, *J. Geophys. Res.*, *102*(A4), 7523–7536.

Liemohn, M., Y. Ma, A. Nagy, J. Kozyra, J. Winningham, R. Frahm, J. Sharber, S. Barabash, and R. Lundin (2007a), Numerical modeling of the magnetic topology near Mars auroral observations, *Geophys. Res. Lett.*, *34*, L24202, doi:10.1029/2007GL031806.

Liemohn, M. W., D. L. Mitchell, A. F. Nagy, J. L. Fox, T. W. Reimer, and Y. Ma (2003), Comparisons of electron fluxes measured in the crustal fields at Mars by the MGS magnetometer/electron reflectometer instrument with a B field-dependent transport code, *J. Geophys. Res.*, *108*(E12), 5134, doi:10.1029/2003JEOO2158.

Liemohn, M. W., et al. (2006), Numerical interpretation of high-altitude photoelectron observations, *Icarus*, *182*(2), 383–395.

Liemohn, M. W., Y. Ma, R. A. Frahm, X. Fang, J. U. Kozyra, A. F. Nagy, J. D. Winningham, J. R. Sharber, S. Barabash, and R. Lundin (2007b), Mars global MHD predictions of magnetic connectivity between the dayside ionosphere and the magnetospheric flanks, in *The Mars Plasma Environment*, pp. 63–76, Springer, New York.

Liemohn, M. W., A. Dupre, S. W. Bougher, M. Trantham, D. L. Mitchell, and M. D. Smith (2012), Time-history influence of global dust storms on the upper atmosphere at Mars, *Geophys. Res. Lett.*, *39*, L11201, doi:10.1029/2012GL051994.

Lillis, R. J., and D. A. Brain (2013), Nightside electron precipitation at Mars: Geographic variability and dependence on solar wind conditions, *J. Geophys. Res. Space Physics*, *118*, 3546–3556, doi:10.1002/jgra.50171.

Lillis, R. J., and X. Fang (2015), Electron impact ionization in the Martian atmosphere: Interplay between scattering and crustal magnetic field effects, *J. Geophys. Res. Planets*, *120*, 1332–1345, doi:10.1002/2015JE004841.

Lillis, R. J., D. L. Mitchell, R. P. Lin, and M. H. Acuña (2008), Electron reflectometry in the Martian atmosphere, *Icarus*, *194*, 544–561, doi:10.1016/j.icarus.2007.09.030.

Lillis, R. J., D. A. Brain, S. L. England, P. Withers, M. O. Fillingim, and A. Safaeinili (2010), Total electron content in the Mars ionosphere: Temporal studies and dependence on solar EUV flux, *J. Geophys. Res.*, *115*, A11314, doi:10.1029/2010JA015698.

Mantas, G. P., and W. B. Hanson (1979), Photoelectron fluxes in the Martian ionosphere, *J. Geophys. Res.*, *84*(A2), 369–385, doi:10.1029/JA084iA02p00369.

Mitchell, D., R. Lin, C. Mazelle, H. Reme, P. Cloutier, J. Connerney, M. Acuña, and N. Ness (2001), Probing Mars' crustal magnetic field and ionosphere with the MGS electron reflectometer, *J. Geophys. Res.*, *106*(E10), 23,419–23,427.

Morgan, D. D., D. A. Gurnett, D. L. Kirchner, J. L. Fox, E. Nielsen, and J. J. Plaut (2008), Variation of the Martian ionospheric electron density from Mars Express radar soundings, *J. Geophys. Res.*, *113*, A09303, doi:10.1029/2008JA013313.

Nielsen, E., et al. (2007), Local plasma processes and enhanced electron densities in the lower ionosphere in magnetic cusp regions on Mars, *Planet. Space Sci.*, *55*(14), 2164–2172.

Němec, F., D. D. Morgan, D. A. Gurnett, F. Duru, and V. Truhlík (2011), Dayside ionosphere of Mars: Empirical model based on data from the MARSIS instrument, *J. Geophys. Res.*, *116*, E07003, doi:10.1029/2010JE003789.

Peterson, W., D. Brain, D. Mitchell, S. Bailey, and P. Chamberlin (2013), Correlations between variations in solar EUV and soft X-ray irradiance and photoelectron energy spectra observed on Mars and Earth, *J. Geophys. Res. Space Physics*, *118*, 7338–7347, doi:10.1002/2013JA019251.

Safaeinili, A., W. Kofman, J. Mouginot, Y. Gim, A. Herique, A. B. Ivanov, J. J. Plaut, and G. Picardi (2007), Estimation of the total electron content of the Martian ionosphere using radar sounder surface echoes, *Geophys. Res. Lett.*, *34*, L23204, doi:10.1029/2007GL032154.

Schunk, R., and A. Nagy (2009), *Ionospheres*, Cambridge Univ. Press, Cambridge, U. K.

Smith, F., and C. Smith (1972), Numerical evaluation of Chapman's grazing incidence integral ch(x, χ), *J. Geophys. Res.*, *77*(19), 3592–3597.

Sung, K., and J. L. Fox (2000), Electron impact cross sections for use in modeling the ionospheres/thermospheres of the Earth and planets, *Eos Trans. AGU*, *81*(48), Fall Meet. Suppl., Abstract SA52A–11.

Trantham, M., M. Liemohn, D. Mitchell, and J. Frank (2011), Photoelectrons on closed crustal field lines at Mars, *J. Geophys. Res.*, *116*, A07311, doi:10.1029/2010JA016231.

Withers, P., and M. Mendillo (2005), Response of peak electron densities in the Martian ionosphere to day-to-day changes in solar flux due to solar rotation, *Planet. Space Sci.*, *53*, 1401–1418, doi:10.1016/j.pss.2005.07.010.

Withers, P., K. Fallows, and M. Matta (2014), Predictions of electron temperatures in the Mars ionosphere and their effects on electron densities, *Geophys. Res. Lett.*, *41*, 2681–2686, doi:10.1002/2014GL059683.

Xu, S., and M. W. Liemohn (2015), Superthermal electron transport model for Mars, *Earth Space Sci.*, *2*(3), 47–64, doi:10.1002/2014EA000043.

Xu, S., M. W. Liemohn, D. L. Mitchell, and M. D. Smith (2014a), Mars photoelectron energy and pitch angle dependence on intense lower atmospheric dust storms, *J. Geophys. Res. Planets*, *119*, 1689–1706, doi:10.1002/2013JE004594.

Xu, S., M. W. Liemohn, and D. L. Mitchell (2014b), Solar wind electron precipitation into the dayside Martian upper atmosphere through the cusps of strong crustal fields, *J. Geophys. Res. Space Physics*, *119*, 10,100–10,115, doi:10.1002/2014JA020363.

Xu, S., M. W. Liemohn, W. Peterson, J. Fontenla, and P. Chamberlin (2015a), Comparison of different solar irradiance models for the superthermal electron transport model for Mars, *Planet. Space Sci.*, *119*, 62–68, doi:10.1016/j.pss.2015.09.008.

Xu, S., M. Liemohn, S. Bougher, and D. Mitchell (2015b), Enhanced carbon dioxide may explain the dust-storm-related increase in high-altitude photoelectron fluxes at Mars, *Geophys. Res. Lett.*, *42*, 9702–9710, doi:10.1002/2015GL066043.

Zhang, M. H. G., J. G. Luhmann, and A. J. Kliore (1990), An observational study of the nightside ionospheres of Mars and Venus with radio occultation methods, *J. Geophys. Res.*, *95*, 17,095–17,102, doi:10.1029/JA095iA10p17095.